RESEARCH ARTICLE

Measurements of a turbulent boundary layer-compliant surface system in response to targeted, dynamic roughness forcing

David Huynh[1] · Beverley McKeon[1]

Abstract

A series of experiments have been performed to study the response of a compliant (gelatin) surface to a turbulent boundary layer that has been forced by dynamic roughness. Through the synthetic flow structure generated by dynamic roughness, this work reduces the complexity of the fluid–structural problem in order to develop a fundamental framework with which to study flow control mechanisms. Flow velocity and surface deformations are measured using 2D particle image velocimetry and stereo digital image correlation, respectively. Both measurement methods are phase-locked to the roughness motion to allow the phase-averaged velocity and deformation fields to be isolated and correlated. The surface response of the non-dynamic roughness forced system is analyzed, and several spectral features are characterized. This analysis is used as context for the roughness forced deformations, subsequently confirming the response of the compliant surface to the synthetic flow mode. This demonstrates the potential of dynamic roughness experiments for studying flow control schemes and sets the stage for more detailed investigations of the effect of the compliant surface on the synthetic flow mode.

Graphic Abstract
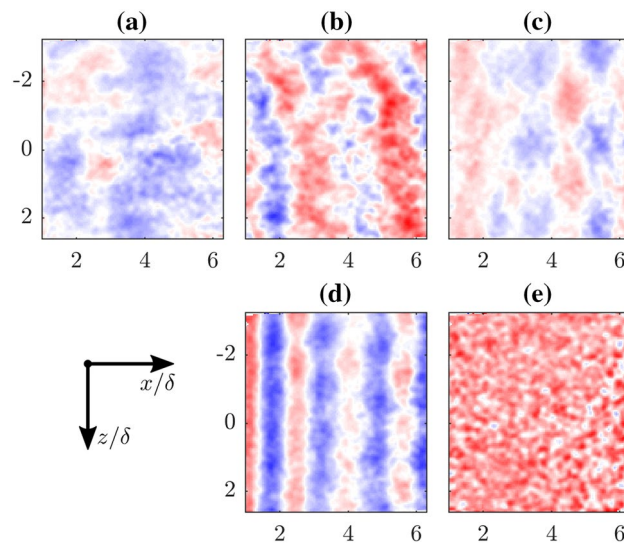
✉ Beverley McKeon
  mckeon@caltech.edu

Extended author information available on the last page of the article

1 Introduction

Since the 1950s, surface compliance has been the subject of research as a potential flow control mechanism (Gad-el Hak 2002). A compliant surface is one that deforms under and modifies the surrounding flow, and in its simplest implementation may offer a passive and cost-effective means of

flow control. Much of the early compliant coating work, including the seminal studies by Kramer (1957), centered around reducing skin friction drag by delaying the onset of turbulence. This inevitably led to the question of whether a compliant coating could be rationally designed to reduce the drag of an already turbulent flow.

Some experimental studies have found encouraging results toward the possible efficacy of these surfaces. Lee et al. (1993) performed water tunnel experiments of a turbulent boundary layer with a single-layer viscoelastic compliant surface and found that the flow structures associated with the near-wall cycle were modified, while the streamwise turbulence intensity and Reynolds shear stress were reduced. In the water tunnel experiments of Choi et al. (1997), drag reduction on a slender body of revolution with a single-layer viscoelastic coating was reported, with a maximum drag reduction of 7%. However, the strain gauge skin friction measurement error was estimated to be as high as $\pm\,4\%$, and so, this drag reduction should be interpreted cautiously. As computational capabilities have grown in recent decades, several DNS studies have been performed with compliant walls and reported somewhat less optimistic results than experiments. Xu et al. (2003) simulated a turbulent channel flow with a compliant wall modeled as a spring-supported plate and found little change to the turbulent skin friction. In the work of Fukagata et al. (2008), an anisotropic compliant wall led to 8% maximum drag reduction rate; however, the drag was found to increase as the computational domain was increased. Kim and Choi (2014) parametrically studied the effect of stiffness of the compliant walls and observed that stiff materials led to minimal changes in the skin-friction drag and coherent structures, while soft materials led to significant drag increase due to resonant surface behavior.

A common observation among these studies is the importance of the interaction between the surface and so-called coherent structures in the flow. Amid the seemingly random perturbations in turbulent flow, coherent structures are regions of strong spatiotemporal coherence that are readily observed in both experiments and simulations and have been found to be energetically and dynamically significant to the turbulent process (Adrian 2007). Further, because these structures exhibit characteristic length scales and convection velocities, their spectral signatures can be fairly narrow and distinct from the otherwise broadband spectrum of turbulence. Thus, they may be approximated as traveling wave disturbances in modeling efforts to capture the key properties of turbulent flows.

One approach born from the concept of coherent structures is to generate a synthetic flow structure and study its resulting interaction with the rest of the flow. Pursuing this, Jacobi and McKeon (2011a) set up a wind tunnel study of a turbulent boundary layer forced by dynamic roughness. Dynamic roughness is a wall roughness element that is temporally actuated in the wall-normal direction, and was found to excite a synthetic, traveling wavelike disturbance into the flow. The subsequent study of Duvvuri and McKeon (2015) observed an interaction between this synthetic scale and triadically coupled small scales that was analogous to the findings of Hutchins and Marusic (2007) involving naturally occurring large-scale coherent structures. A summary of the results obtained by these authors using dynamic roughness in turbulent boundary layers can be found in McKeon et al. (2018).

Subsequently, Huynh and McKeon (2019) used particle image velocimetry (PIV) to perform a parametric characterization of the spatiotemporal structure of the synthetic scale induced by dynamic roughness operating over a range of frequencies and amplitudes. The study identified the streamwise spatial wavelength of the phase-averaged streamwise and wall-normal response of the boundary layer, which was previously inferred only for the streamwise component from temporal data using Taylor's hypothesis. A reasonably clean and streamwise persistent signature of a coherent traveling wave structure was observed for all but the highest actuation frequency condition. The streamwise decay and modulation of the synthetic response were characterized, and its essentially two-dimensional nature (spanwise constant, with a slight bow, or phase advance at spanwise locations corresponding to the ends of the roughness element) was confirmed.

The current work aims to study the response of a compliant surface to a single-scale, traveling wavelike, dynamic roughness forced flow structure in a turbulent boundary layer. This approach is motivated by the dynamical significance of coherent structures in canonical and compliant wall turbulent flows, and leverages the synthetic mode generated by dynamic roughness to provide a deterministic input, and thus overcome one of the challenges associated with correlating surface response with turbulence stimulation. Rather than identifying a surface that achieves a particular performance goal such as turbulent drag reduction, this study seeks to investigate the measurable response (beneficial or not) of a simple compliant surface to a well-characterized input. Even obtaining a measurable response can be challenging given the wide parameter space spanned by both turbulent fluctuations and material behavior. This input–output-type analysis intends to reduce the complexity of the problem and provide a fundamental framework with which to build up to the full flow, consistent with the related resolvent modeling approach for compliant surfaces outlined in Luhar et al. (2015). The ultimate goal of this line of study is the demonstration of the efficiency of such compliant wall resolvent modeling when applied to this single, narrow-band synthetic disturbance, which will enable a more detailed interpretation of the existing and new literature on compliant walls in turbulent boundary layer, and identify from the equations

of motion which material properties (if any) could lead to a net drag reduction. This is out of the scope of the present effort, however, which focuses on a compliant surface with properties designed to demonstrate a response to a turbulent boundary layer which is dynamically forced with a single synthetic scale in addition to the background turbulence.

To accomplish this, the dynamic roughness apparatus was adapted to a flat plate turbulent boundary layer experiment in a water tunnel. A gelatin sample was embedded in the flat plate just downstream of the roughness element. Measurements were taken of the flow velocity using 2D PIV and the surface deformations using stereo digital image correlation (DIC). Surface displacements with and without the forcing were analyzed, and a response due to the synthetic flow mode was confirmed. For convenience, the rigid wall and compliant wall cases are referred to as 'RW' and 'CW,' respectively, and the dynamic roughness forced and non-forced cases referred to as 'DRF' and 'unforced,' respectively. It is recognized that 'unforced' cases without roughness forcing are still being driven by the flow. The goals of this article are to describe the experiments performed and present the results of the surface deformation measurements; a thorough discussion of the velocity fields is reserved for another instance. In what follows, the experimental and analytical details of the study are outlined in Sect. 2. In Sect. 3, several results are discussed. The turbulent statistics and phase-averaged PIV fields are briefly compared for the RW-DRF and CW-DRF campaigns. A spectral and spatial analysis of the DIC data from the CW-unforced study is performed to identify naturally occurring wave structures in the gelatin sample. This is compared with DIC data from the CW-DRF experiment, and the interaction with the synthetic flow mode is verified and characterized. We conclude in Sect. 4.

2 Approach

A complete description of the rigid wall, dynamic roughness experiments, PIV setup, and phase-averaged and Fourier decomposition is given in Huynh and McKeon (2019). Here, those elements are summarized and emphasis is placed on the implementation of the compliant surface, the DIC apparatus, and spectral analysis for the deformation data.

2.1 Experimental setup

The experiments were performed in the NOAH water tunnel at Caltech. An illustration of the experiment is shown in Fig. 1; note that the schematic is vertically reflected with respect to the physical setup, i.e., measurements were taken on the bottom surface of the flat plate. The flow was tripped at the leading edge of the acrylic plate to promote a turbulent boundary layer. A thin, spanwise constant aluminum rib served as the roughness element located 63 cm downstream of the leading edge, actuated perpendicularly to the plate by a Bose ElectroForce 200 N motor. The origin of the x-axis for subsequent observations was fixed at the downstream edge of the rib, and x is normalized by the boundary layer thickness at this location. The compliant sample was embedded into the acrylic plate with the leading edge 21.2 mm downstream of the roughness element (at $x/\delta = 0.83$), as discussed in more detail shortly. The properties of the canonical flow (rigid wall, unforced) are summarized in Table 1, acquired from PIV at the roughness location. In Table 1,

Table 1 Flow properties for the canonical flow (rigid wall, unforced), acquired from PIV at the roughness location

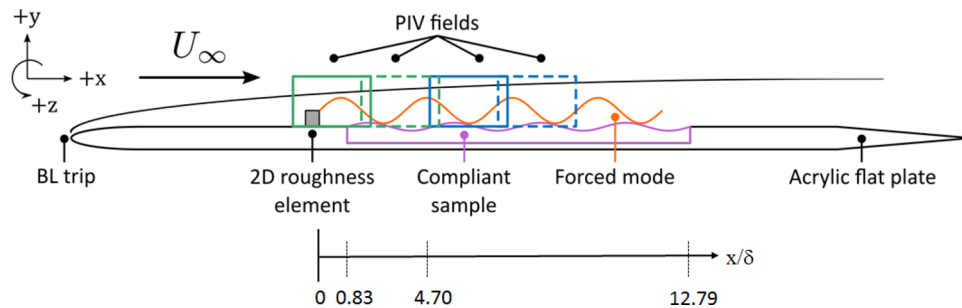| U_∞	u_τ	δ	δ_ν	Re_θ	Re_τ
33 cm/s	1.6 cm/s	25.5 mm	62.5 μm	870	410

Fig. 1 Illustration of the experimental setup. The rectangles representing the PIV fields are not true to scale or aspect ratio, but are shown to represent the FOVs of the two cameras and the streamwise shift between setups required to obtain the long spatial field of view reported here. Data were acquired with the cameras in the green FOVs and then separately in the blue FOVs. The phase-averaged vector fields were stitched together in post-processing. The x/δ locations of the LE and TE of the compliant panel and the station at which the mean statistics are reported are also shown

the friction velocity, $u_\tau = \sqrt{\tau_w / \rho}$, was estimated using the Clauser chart method (Fernholz and Finley 1996), and the viscous length scale, $\delta_v = \nu / u_\tau$, and friction Reynolds number, $\mathrm{Re}_\tau = u_\tau \delta / \nu$, were calculated accordingly.

The roughness element was actuated sinusoidally at a range of amplitudes and frequencies. The motion is described by equation 1:

$$h(t) = \frac{h_{\mathrm{rms}}}{\sqrt{2}} \left[-\cos\left(2\pi\omega_{\mathrm{f}}t\right) + 1 \right], \tag{1}$$

where $h = 0$ corresponds to the rib flush to the wall, ω_{f} is the angular frequency of actuation, and h_{rms} is the rms amplitude of the motion. The roughness is actuated at three frequencies, $f_{\mathrm{f}} = [3, 5, 10]$ Hz or $\omega_{\mathrm{f}} = [1.4, 2.4, 4.8]\, U_\infty / \delta$, at an rms amplitude of 1.1 mm or 0.042δ, and at an increased rms amplitude of 1.8 mm or 0.069δ at 5 Hz. These actuation conditions are summarized in Table 2 and labeled i–iv for reference. The conditions were selected to have a comparable amplitude to that of Duvvuri and McKeon (2015), with order-of-magnitude higher dimensionless frequencies to generate shorter synthetic structures.

Gelatin was chosen as the compliant material for this study due to its low cost, ability to be made very soft, and nearly linearly elastic behavior for small deformations (Gad-el Hak 1986). It is reemphasized here that the goal of this work was not to achieve a particular performance metric (e.g., drag reduction), but rather to elicit and study a measurable surface response to the synthetic structure generated by the dynamic roughness. To that end, it was key that the material be sufficiently soft to promote detectable deformations. Additionally, the linear elastic behavior of gelatin was ideal to facilitate the modeling of the surface's behavior.

Table 2 Roughness actuation conditions (i–iv) explored in these experiments, parameterized by motion rms height and frequency

	h_{rms}/δ [h_{rms}]	
	0.042 [1.1 mm]	0.069 [1.8 mm]
$\frac{\omega_\mathrm{f}\delta}{U_\infty}$ [f_{f}]		
1.4 [3 Hz]	i	–
2.4 [5 Hz]	ii	iii
4.8 [10 Hz]	iv	–

The rms heights and frequencies are given in outer-scaled non-dimensional form [with the dimensional values in brackets]. The corresponding inner-scaled values (based on u_τ in the rigid wall, unforced case at x/δ corresponding to the roughness location) are $h^+ = 17, 28$ and $\omega_{\mathrm{f}}^+ = 0.070, 0.12, 0.24$, respectively

The compliant samples were fabricated by adding boiling water to simple gelatin powder (Knox, unflavored), thoroughly mixing the two with an emulsion blender, pouring the mixture into a mold, and allowing the gelatin to cool at room temperature. Care was taken to minimize bubbles and gelatin clumps in the solution. A gelatin-to-water ratio of 4:100 was used, which was near the determined minimum ratio for which a cohesive solid still formed. The gelatin was molded directly into an acrylic plate section that integrated with the flat plate facility, as illustrated in Fig. 1. The sample was molded to be 305 mm long × 25.4 mm deep × 343 mm wide ($12.0 \times 1.00 \times 13.5\ \delta^3$ or $4880 \times 410 \times 5490\ \delta_v^3$), to match the roughness element's spanwise length and reduce edge effects along the centerline of the sample.

A series of Instron 5500 compression tests were performed on several gelatin samples and the resulting Young's modulus was estimated to be 4.5 kPa ($\pm$ 0.2 kPa), which was consistent with values reported by Gad-el Hak (1986). This is extremely compliant; for comparison, the PDMS studied by Zhang et al. (2015) had a Young's modulus of $\sim$ 1 MPa. It is noted that while these simple compression tests may not have been as accurate as other methods, e.g., tensile tests, they were suitable for an estimate of the elastic properties, particularly for such a soft material. The Poisson's ratio, ν_s, was assumed to be 0.5, i.e., the material was assumed incompressible (e.g., Czerner et al. 2015). With two elastic moduli known, the remaining elastic properties are determined for a homogeneous, isotropic, linear elastic material. Of particular relevance is the shear modulus, G, which determines the shear or transverse wave speed of the solid, U_s:

$$G = \frac{E}{2(1 + \nu_s)} \sim 1.4\ \text{kPa} \tag{2}$$

$$U_s = \sqrt{G/\rho_s} \sim 1.2\ \text{m/s}, \tag{3}$$

where ρ_s is the density of the gelatin (taken to be the same as water due to the mixture ratio). The shear wave speed was significantly higher than the freestream velocity ($\sim$ 0.3 m/s), and thus, hydroelastic instability waves were not expected (Gad-el Hak 1986). Other relevant wave speeds to consider were the Rayleigh wave speed (Freund 1998), the generalized Rayleigh wave speed (Bolt and Butcher 1960), and the Love wave speed (Fung 1965). The former pertains to surface waves on a semi-infinite elastic solid, while the latter two consider the finite thickness of the gelatin sample. For the material investigated, the Rayleigh, generalized Rayleigh, and Love wave speeds were calculated to be 1.15, 1.18, and 1.32 m/s, respectively, assuming the gelatin to be incompressible and incorporating the sample geometry and observed deformation wavelengths.

2.2 Diagnostics

Two-component, planar PIV was performed to obtain streamwise and wall-normal velocity fields (u and v, respectively), using two cameras, each positioned at two streamwise locations, to resolve the long streamwise extent of the synthetic mode. Images were acquired with two Phantom Miro LAB 320 high-speed cameras, each equipped with an AF Micro-NIKKOR 200m f/4D Nikon lens. Each camera field of view (FOV) was $2.1 \times 1.3\delta^2$, arranged to have a 0.2δ overlap with the next streamwise FOV to allow for accurate stitching between windows, as shown in schematic in Fig. 1. To have sufficient phase resolution over the actuation period, the camera frame rates were set 20 times higher than the actuation frequency, 60–200 Hz or $4.6-15.5\ U_\infty/\delta$. For the unforced cases, the frame rate was set to 100 Hz or $7.7\ U_\infty/\delta$. The streamwise wall-normal FOV was illuminated by a laser sheet brought up through the bottom of the test section. The images were acquired and processed using LaVision's DaVis software.

Stereo-DIC measurements taken made to obtain two-dimensional, three-component surface deformations of the gelatin sample, referred to as d_x, d_y, and d_z for the streamwise, wall-normal, and spanwise deformations, all of which are functions of the streamwise and spanwise coordinates as well as time. A photograph of the setup is shown in Fig. 2. Two Photron Fastcam APS-RS cameras were used; each equipped with an AF NIKKOR 50mm f/1.8D Nikon lens. Images were acquired at full resolution, $1024 \times 1024\text{pixel}^2$, and at a frame rate 20 times the roughness actuation frequency and 100 Hz for the unperturbed case, as for the PIV. The cameras were positioned under the test section, at a $22°$ viewing angle to the FOV and the lens apertures closed
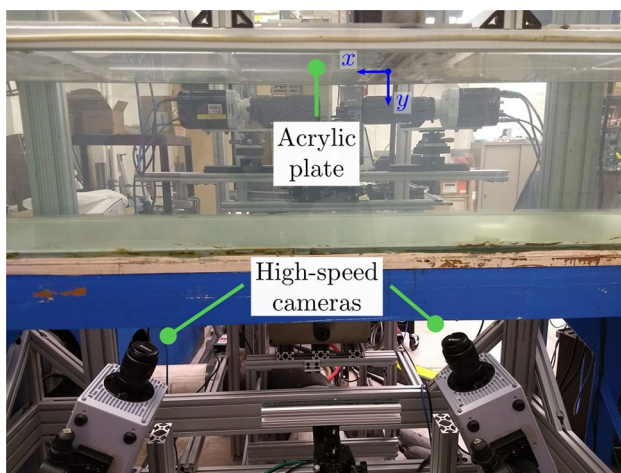
enough to maintain focus over the entire FOV. The gelatin sample was frontlit via an LED flood lamp. The images were acquired and processed in DaVis, using a least squares matching (LSM) method with 7 seeding points, a subset size of 31×31 pixel^2 and a step size of 8 pixel, and built-in 'medium' calculation mode.

DIC measurements were taken from the x–z plane coincident with the gelatin surface. Data were taken in three locations, as illustrated in Fig. 3a: a leading-edge (LE) FOV, aligned to capture the upstream edge of the sample and roughly centered on the centerline; a corner FOV, capturing the upstream, $-z$ corner of the sample; and a trailing-edge (TE) FOV, capturing the downstream edge of the sample and roughly centered on the centerline. The streamwise–spanwise dimensions for the three FOVs were roughly 133×147 mm^2 ($5.2 \times 5.8\ \delta^2$ or $2100 \times 2300\ \delta_v^2$); note these were not square because the acrylic plate masked a portion of the streamwise dimension.

The speckle pattern for DIC was applied using a Flairosol spray bottle and black India ink. The spray bottle created a fine mist from the ink, which settled onto and stained the gelatin surface, forming a pattern such as the one shown in Fig. 3b. This speckle pattern had good contrast, 3–5 pixel speckle features, randomness, and isotropy, though the speckle density was slightly less than the ideal 50%. This was unavoidable, as spraying too much ink led to the formation of large droplets. Still, this pattern was found to yield good DIC results and the application method avoided damage to the ultra soft and wet gelatin sample, which occurred with more traditional methods such as stamp rollers and spray paint.

The DIC was calibrated using a LaVision type 58-5 stereo calibration plate and resulted in a standard deviation of fit of < 0.1 pixels. The average uncertainties on the streamwise,

Fig. 2 Photograph of stereo-DIC camera setup. The two cameras were positioned under the test section, at an angle of $22°$ from the normal
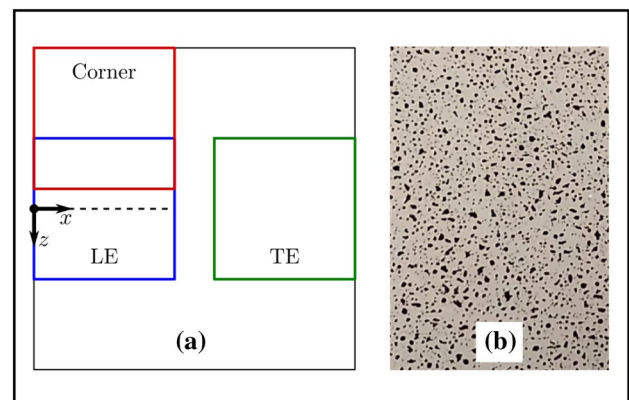

Fig. 3 **a** Diagram of the three FOV locations for the DIC study: leading edge (LE), corner, and trailing edge (TE). The black dashed line indicates the location of the PIV FOVs. **b** Photograph of the speckle pattern generated with a fine mist water bottle and black India ink. The photograph dimensions are 27×40 mm^2

wall-normal, and spanwise displacements were 0.3, 0.3, and 0.2 μm, respectively, based on errors associated with variation in the speckle pattern applied to the surface, illumination and viewing angle and as obtained from DaVis. In addition, the noise floor was estimated by processing a record of the stationary sample. The average noise floor for the streamwise, wall-normal, and spanwise displacements was 0.5, 1.4, and 0.5 μm, respectively.

2.2.1 Phase locking

Both the PIV and DIC measurements were phase-locked to the roughness motion, allowing their statistics and phase-averaged quantities to be correlated. This was accomplished through a series of synchronized clock signals generated by a National Instruments PCIe-6321 DAQ card and the MATLAB DAQ Toolbox. For data acquired at phase index $j \in [0, 19]$ of the actuation period (corresponding to the frame rate being 20 times the actuation frequency), the corresponding height of the roughness is described by Eq. 4:

$$h_j = \frac{h_{\mathrm{rms}}}{\sqrt{2}}\left[-\cos\left(2\pi\frac{j}{20}\right) + 1\right], \tag{4}$$

with $j = 0$ corresponding to the roughness flush to the wall. To minimize frequency drift during an acquisition, the actuation frequency was determined to within 0.01 mHz and used to set the clock signal frequencies. Over a typical record of $\sim$ 2000 images, the clock and encoder signal remained synchronized to within 0.015% of the actuation period.

2.3 Analysis tools

2.3.1 Phase-averaged and Fourier decomposition

To analyze the velocity and deformation measurements, we first employ the triple decomposition of Hussain and Reynolds (1970):

$$\phi(\mathbf{x}, t) = \overline{\phi}(\mathbf{x}) + \widetilde{\phi}(\mathbf{x}, \omega_{\mathrm{f}}t) + \phi'(\mathbf{x}, t) \tag{5}$$

where $\overline{(\cdot)}$ denotes a temporal mean (estimated by an ensemble average), $\widetilde{(\cdot)}$ denotes a phase average, and $(\cdot)'$ denotes the perturbation about the combined mean and phase-averaged quantity. The focus of the analysis will be concerned with the phase-averaged quantities, as these are the components temporally coherent with the roughness actuation.

The phase averaging process is directly related to temporal Fourier analysis. Thus, it is natural to employ a discrete Fourier transform (DFT) in time to further decompose the flow fields into a fundamental component corresponding to ω_{f} and its harmonics:

$$\widetilde{\phi}(\mathbf{x}, \omega_{\mathrm{f}}t) = \sum_m \hat{\phi}_{m\omega_{\mathrm{f}}}(\mathbf{x})e^{-im\omega_{\mathrm{f}}t} + \text{c.c.}, \tag{6}$$

where $\hat{\phi}_{m\omega_{\mathrm{f}}}$ are the temporal Fourier modes and 'c.c.' stands for complex conjugate to recover a real physical quantity. The $m = 1$ mode corresponds to the forcing frequency component, $\hat{\phi}_{\omega_{\mathrm{f}}}$, and the physical quantity reconstructed by this component is denoted by $\phi_{\omega_{\mathrm{f}}}$. This process isolates the portion of ϕ that is coherent specifically with ω_{f}.

The synthetic flow structures generated by dynamic roughness have been shown to have a well-defined streamwise wavenumber, $k_{x\mathrm{f}}$ (Huynh and McKeon 2019). Although the parallel flow assumption does not strictly hold, studying the $k_{x\mathrm{f}}$-coherent component of the flow and surface response proves useful. Once $k_{x\mathrm{f}}$ was estimated, the ω_{f}-temporal Fourier modes, $\hat{\phi}_{\omega_{\mathrm{f}}}$, were discrete Fourier transformed in x:

$$\hat{\phi}_{\omega_{\mathrm{f}}}(x) = \sum_n \hat{\hat{\phi}}_{\omega_{\mathrm{f}}nk_{x\mathrm{f}}}e^{ink_{x\mathrm{f}}x}, \tag{7}$$

where $\hat{\hat{\phi}}_{\omega_{\mathrm{f}}nk_{x\mathrm{f}}}$ are the spatiotemporal Fourier modes. Here, a zero padding in x has been performed such that $k_{x\mathrm{f}}$ is a multiple of the lowest resolved wavenumber, i.e., a total-energy-preserving spectral interpolation has been applied to ensure $k_{x\mathrm{f}}$ is a resolved wavenumber. The index $n = k_x/k_{x\mathrm{f}}$ is determined by this process and by construction includes $n = 1$. Analogously to the temporal Fourier modes, the $n = 1$ mode corresponds to the $\omega_{\mathrm{f}}-k_{x\mathrm{f}}$ spatiotemporal Fourier component of ϕ. This mode and its physical reconstruction are denoted $\hat{\hat{\phi}}_{\omega_{\mathrm{f}}k_{x\mathrm{f}}}$ and $\phi_{\omega_{\mathrm{f}}k_{x\mathrm{f}}}$, respectively.

This analysis procedure was applied to both the velocity (u and v) and the deformation fields (d_x, d_y, and d_z). Note that the velocity data were acquired in an x–y plane, while the deformations were acquired an x–z plane. It follows that the temporal and spatiotemporal Fourier modes for the quantities are functions of y and z, accordingly.

2.3.2 Power spectral density estimation and temporal Fourier band-pass filtering

It was necessary to characterize the broadband energetic spectral features in the compliant surface deformations in order to determine the response to the dynamic roughness forced flow structure. To identify the spectral features in the unforced surface deformations, temporal power spectral densities (PSDs) were calculated from single DIC records using Welch's method in MATLAB, with 10 windows and 50% overlap. The DIC records were 2047 samples long and acquired at 100 Hz. The PSDs were calculated for each deformation component, at each x and z spatial position in the data. The spectra were then averaged over x and z (removing the top and bottom 5% values) to arrive at a representative PSD for a given deformation component in a given FOV.

As will be discussed, the power spectra revealed several energetic frequency bands in the unforced deformations. The spatial structure corresponding to each of these spectral features was explored by discrete Fourier band-pass filtering the deformation signal over the corresponding frequency band. This was performed on the same 2047 sample length, 100 Hz DIC records as the PSDs. A Fourier band-pass filtered signal is denoted with a subscript $\omega_{(\cdot)}$, with $(\cdot)$ replaced by the feature name; for example, the wall-normal deformation, Fourier filtered for feature A is denoted $d_{y|\omega_A}$.

3 Results and discussion

3.1 Mean flow statistics and flow response to DRF

Figure 4 presents a comparison of the mean flow statistics for the rigid wall and compliant wall dynamic roughness forced flows for actuation condition iii, along with the canonical flow. All profiles are taken at the $x/\delta = 4.7$ station in the PIV.

In Fig. 4a, the RW- and CW-DRF mean profiles are seen to agree well, with both exhibiting a deficit relative to the canonical case for $0.07 < y/\delta < 0.6$. Likewise in Fig. 4b, the RW and CW turbulence intensities and Reynolds shear stress match closely, with all profiles indicating elevated energetics over the canonical flow. Some deviation can be seen in the streamwise turbulence intensities near the wall, as the CW u_{rms} peak has shifted nearer to the wall to an unresolved y location. The rigid wall, DRF data were previously shown to be consistent with the static roughness studies of Jacobi and McKeon (2011a, b), who observed internal layers forming within the boundary layer, originating from the smooth-to-rough and rough-to-smooth transition points at the wall. As the CW-DRF profiles are in close agreement with those of the RW-DRF study, it appears that the addition of the compliant wall had a minimal effect on the mean properties of the roughness forced flow. This suggests that even though the gelatin sample is very soft (Young's modulus of 4.5 kPa), the inertia of the flow was insufficient (i.e., the Reynolds number was too low) to cause deformations large enough to couple back to the flow statistics. Such interaction where the flow influences the surface but vice versa is referred to as one-way coupling and is found to occur for wall deformations of less than 1 viscous unit (Zhang et al. 2017; Benschop et al. 2019). However, this definition of one-way coupling refers to the mean properties of the flow; there may still be an $\omega_f - k_{xf}$-coherent interaction whereby the compliant surface affects the synthetic flow mode.

Figure 5 shows phase snapshots ($j = 0$ in Eq. 4) of the ω_f Fourier reconstructed velocity fields, ϕ_{ω_f}, from the RW- and CW-DRF studies (actuation condition iii); see supplemental material for the temporal evolution of these velocity
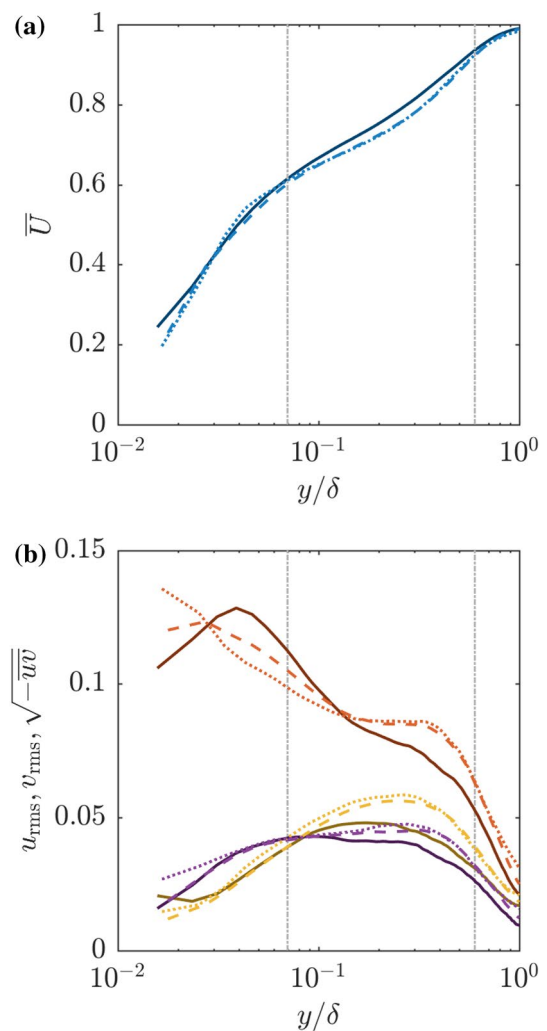

Fig. 4 Comparison of the RW-DRF, CW-DRF (both from actuation condition iii), and canonical mean flow statistics ($x/\delta = 4.7$): **a** mean streamwise velocity (blue), **b** streamwise (red) and wall-normal (yellow) turbulence intensities, and Reynolds shear stress (purple). Line styles are as follows: (solid) canonical, (dashed) RW-DRF, (dotted) CW-DRF. The vertical dash dotted lines indicate $0.07 < y/\delta < 0.6$. All velocities are non-dimensionalized by U_∞

fields. Red and blue shading indicates high and low speed, respectively, and $x = 0$ corresponds to the roughness location. Both sets of velocities exhibit a clearly streamwise periodic structure, i.e., the synthetic mode. Though not evident from a single snapshot, the synthetic mode convects downstream with a constant convection velocity of $0.83U_\infty$ (RW) or $0.80U_\infty$ (CW), while gradually decaying and slowly drifting away from the wall in each case. As with the flow statistics, the CW synthetic structure is nearly identical to that of the RW: u_{ω_f} undergoes a sharp π phase jump in y, resulting in a four-lobe pattern in one spatial period; v_{ω_f} is very tall and straight in y and instead has a two-lobe pattern. The wall-normal phase variation of the RW and CW modes appears to agree quite closely as well; in each case,

Fig. 5 Phase snapshots ($j = 0$) of phase-averaged, ω_f coherent **a** streamwise (u_{ω_f}) and **b** wall-normal (v_{ω_f}) fluctuating velocities. For each velocity component, the rigid wall data are given on top and the compliant wall on bottom. All data correspond to actuation condition iii. The velocities are non-dimensionalized by U_∞ and the contour shading limits are $[-0.2, 0.2]$. See supplemental material for the temporal evolution of these velocity fields
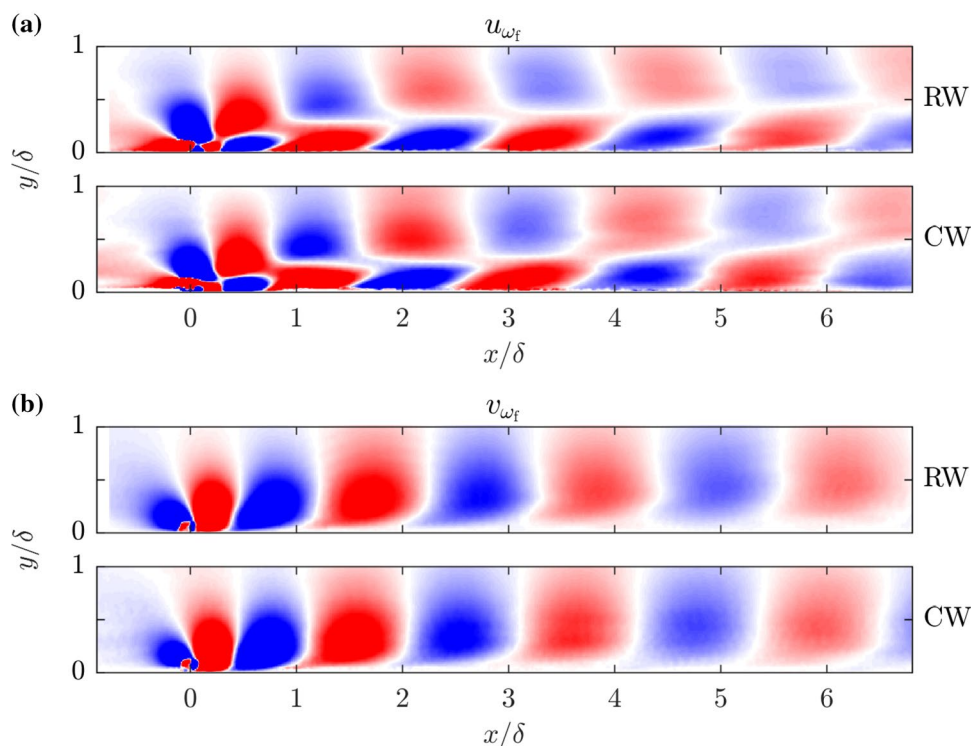
the wall-normal phase behavior of u_{ω_f} and v_{ω_f} is consistent with a two-dimensional perturbation, which was experimentally confirmed by a series of spanwise parallel PIV measurements (Huynh and McKeon 2019). Once again, the compliant wall had little impact on the general shape and character of the roughness forced flow structure. However, close inspection of the downstream region shows that the CW synthetic mode begins to lag slightly behind the RW mode. This is a result of the compliant wall structure having a slightly shorter wavelength (and correspondingly lower convection velocity). This observation along with a more thorough analysis of the velocity fields is reserved for another instance in favor of a comprehensive discussion of the surface deformations, namely verification and characterization of the surface response to the synthetic flow mode.

3.2 Surface response of the elastic compliant wall to an unforced turbulent boundary layer

Before analyzing the compliant wall's response to the dynamic roughness forcing, the response of the gelatin sample to the unforced turbulent boundary layer flow was studied. This was done by submerging the compliant sample in the test section, fixing the roughness element to be flush with the wall, and running the water tunnel. The characterization of the unforced system is important to determine whether the synthetic mode directly causes a surface response, or simply amplifies a naturally occurring mode. The streamwise, wall-normal, and spanwise deformation fields, d_x, d_y, and d_z,

respectively, discussed here are temporally mean subtracted and are each functions of x, z, and t. For a sense of scale, the rms values for the LE FOV deformations taken over x, z, and t are given in Table 3. For reference, the uncertainty values on the stereo-DIC calculation were 0.3, 0.3, and 0.2 μm for d_x, d_y, and d_z, respectively. The deformation distributions are essentially Gaussian, with the vast majority of the displacements within three times the rms value for a given component. Thus, the instantaneous displacements are generally resolvable. They are, however, small ($< 10\%$) compared with the viscous length scale.

The averaged PSDs for d_x, d_y, and d_z in the LE FOV are plotted in Fig. 6a. The streamwise and wall-normal deformation spectra appear to have significant content in similar frequency bands, and the spanwise deformation spectrum shows similar activity at a reduced intensity for this FOV. The averaged PSDs for d_y for each of the three FOVs are plotted in Fig. 6b. Several spectral features are clearly highlighted, and a brief discussion of five select frequency bands

Table 3 Rms values of each deformation component for the LE FOV of the CW-unforced study, provided in dimensional, outer-scaled, and inner-scaled forms

	d_x	d_y	d_z
rms($\cdot$) [um]	4.2	4.0	2.6
rms($\cdot$)/δ	1.6×10^{-4}	1.6×10^{-4}	1.0×10^{-4}
rms($\cdot$)/δ_v	0.07	0.06	0.04

will be given. For reference, each frequency band/feature will be named A–E in order of increasing frequency content, per Table 4 and the labels in Fig. 6b. Snapshots of the band-pass filtered wall-normal deformations are shown in Fig. 7 for each of the features considered; see supplemental material for the temporal evolution of these deformation fields, and particularly the relative convection velocities. The d_y deformation component was selected due to its prominence in all of the spectral features, as it is the strongest or comparable to the strongest deformation for each frequency band. Given the significance of d_y and in anticipation of a strong relationship to the wall-normal velocity near the wall, this component was the focus of the present analysis. This also serves to narrow the otherwise very broad scope of the data. Details of the other deformations are given in the text when relevant. A more complete three-component analysis is provided in Huynh (2019).

Feature A (Fig. 7a) sits in a low, 0–3 Hz frequency band and is present in all three deformation components in all three FOVs. The amplitude of the peaks for d_x and d_z is fairly uniform in the FOVs, but is significantly higher in the TE for d_y. Large spatial structures are observable in $d_{x|\omega_A}$ and $d_{y|\omega_A}$, and somewhat less so in $d_{z|\omega_A}$. The $d_{y|\omega_A}$ deformations are the highest amplitude of the three components. These large
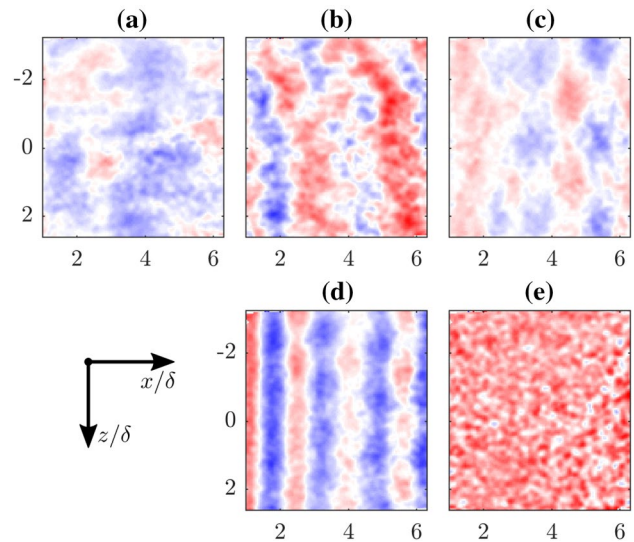

Fig. 7 Snapshots of the Fourier band-pass filtered wall-normal deformation field (d_y) for features A–E (a–e, respectively) from Fig. 6b. Data shown are for the leading-edge FOV. The contour shading limits vary for visibility and are (in μm): **a** [− 6.0, 6.0], **b** [− 2.0, 2.0], **c** [− 9.0, 9.0], **d** [− 3.0, 3.0], **e** [− 2.0, 2.0]. See supplemental material for the temporal evolution of these deformation fields

Table 4 Names and corresponding frequency bands for the spectral features in the CW-unforced deformations from Fig. 6, given in dimensional, outer-scaled, and inner-scaled forms

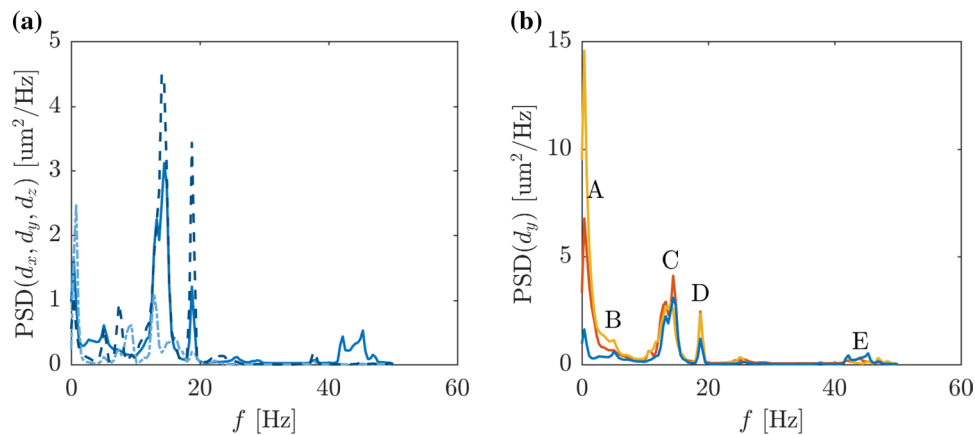| Feature	A	B	C	D	E
f [Hz]	0–3	4.5–5.5	11–16	18.3–19.3	41–45
$f\delta/U_\infty$	0–0.23	0.35–0.43	0.85–1.24	1.41–1.49	3.17–3.48
$f\delta_v/u_\tau$	0–0.012	0.018–0.022	0.043–0.063	0.072–0.075	0.16–0.18

Fig. 6 Temporal power spectra (spatially averaged) of the compliant wall deformations in response to the unforced turbulent boundary layer. **a** Power spectra for all three deformation components from the leading-edge FOV: d_x (dark blue, dashed line), d_y (blue, solid line), and d_z (light blue, dash dotted line). **b** Power spectra for the wall-normal deformation, d_y, for each FOV: leading edge (blue), corner (red), and trailing edge (yellow). Particular spectral features are labeled A–E in (**b**) for reference in the discussion

structures are observed to convect downstream very slowly. Because of its very low-frequency content, it is possible that this feature is driven by the mean shear, with the surface slowly deforming and restoring. Another possible driver may be the near-wall cycle (NWC), which is often characterized by the inner-scaled wavelength and wave speed of $(\lambda_x^+, c^+) = (1000, 10)$. This converts to an inner-scaled frequency of $f^+ = 0.01$, which equates to $f = 2.6$ Hz for these flow conditions. However, while this does fall within the frequency range for feature A, the structures generally appear more spanwise/obliquely aligned than the quasi-streamwise vortices typical of the NWC.

Feature B (Fig. 7b) is a small peak near 5 Hz. It is examined not because of its energetic content, but because it resides near the 5 Hz forcing frequency for actuation conditions ii and iii, which are the focus of the results presented later. The peak of feature B is present in all three deformation components and all three FOVs, and is slightly higher for d_y. Though the peak is made somewhat broad in Fig. 6b by the window averaging process, taking the windows to be the full record length to maximize the spectral resolution resolves the peak location at 5.2 Hz, clearly distinct from the precise 5 Hz forcing of the Bose motor. $d_{y|\omega_B}$ contains well-defined structures that are nearly spanwise-aligned. These $d_{y|\omega_B}$ structures are seen to convect downstream, occasionally organizing into distinct spanwise constant, streamwise traveling waves, and then quickly breaking up. Given the downstream directionality of these structures, it is likely that they are flow driven. Their semi-spanwise alignment may indicate origins from the rigid-to-compliant transition at the upstream edge of the sample. Notably, neither $d_{x|\omega_B}$ nor $d_{z|\omega_B}$ exhibit these semi-spanwise-aligned structures.

Feature C (Fig. 7c) is the broadband spectral content observed for 11–16 Hz in Fig. 6b. Here, we see strongly coherent structures in $d_{y|\omega_C}$, as well as $d_{x|\omega_C}$ and $d_{z|\omega_C}$ (not shown), for all FOVs. $d_{y|\omega_C}$ is seen to exhibit streamwise waves with a distinct spanwise modulation. To develop a more complete picture of the wave system composing this frequency band, snapshots of feature C in each of the three FOVs are shown in Fig. 8. Inspection of the corner FOV highlights the spanwise modulation on top of the dominant streamwise waves. While the modulation has weakened in the TE FOV, it is still discernible. It is particularly clear in temporal animations of the data that the waves are generated at the boundaries of the sample and tend to travel toward the compliant sample's center, i.e., spanwise waves emanate from the spanwise edges and move toward $z = 0$, while the streamwise waves emanate from the up- and downstream edges and travel toward $x/\delta = 7$. This strongly suggests that a geometry-dependent mechanism is involved, imprinting the sample's rectangular geometry into the surface response. The energy for this frequency content may come from natural vibration modes of the plate/support structure. Though not directly comparable to the study of Gad-el Hak (1986) on instability waves in an elastic surface, these waves do share the features of being relatively symmetric and quite low amplitude. The average wave speed of the streamwise waves was estimated to be ∼ 80 cm/s, significantly lower than the gelatin's shear and Rayleigh wave speeds (120 and 115 cm/s, respectively). It is possible and perhaps likely that the material's shear wave speed was not estimated with sufficient accuracy given the extreme softness of the material and simple compression tests performed. Additionally, it is almost certain that the material's properties would have changed after being submerged in the water tunnel for multiple days, likely further softening it and reducing its shear wave speed.

Feature D (Fig. 7d) is a large peak centered at $f = 18.8$ Hz in Fig. 6b. The peak amplitude is highest for d_x in all of the FOVs and is strongest for all components
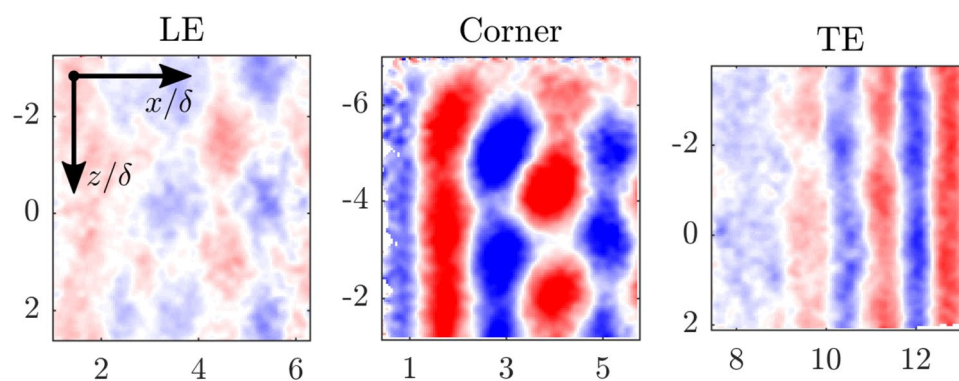

Fig. 8 Snapshots of the Fourier band-pass filtered wall-normal deformation field for spectral feature C, $d_{y|\omega_C}$: (left) leading-edge FOV, with streamwise waves propagating downstream and spanwise waves propagating toward $z = 0$; (center) corner FOV, with streamwise waves propagating downstream and spanwise waves propagat-ing toward $z = 0$; (right) trailing-edge FOV, with streamwise waves propagating upstream. All contour shading limits are [− 9.0, 9.0] μm. See supplemental material for the temporal evolution of these deformation fields

at the TE. There are very strong similarities between the structure of features D and C, both containing distinct streamwise and spanwise waves. Though not shown here, the similarities extend to all three FOVs. Notably, feature D appears to contain slightly higher-wavenumber content than C. Given the slightly higher-frequency band of D, this is consistent with the two features having similar wave speeds. The structural similarity suggests that features C and D may share a geometry-dependent mechanism that dictates their spatial coherence. The 18.8 Hz frequency of feature D matches very well with the tunnel pump frequency of 18.94 Hz, so it is likely that the energy for this feature is derived from oscillations induced by the pump. However, the mechanism through which these oscillations transmit to the gelatin is not obvious, whether through the water, by flow-driven vibrations of the plate structure, or by structural vibrations directly from the pump.

Feature E (Fig. 7e) resides in the 41–46 Hz frequency band, nearer to the 50 Hz Nyquist limit than the other features. Though not as apparent as some of the other features, there is some broadband content appearing in this frequency range. Looking at $d_{y|\omega_E}$, the deformation is uniformly incoherent and appears noise-like. Thus, this content may be the result of some source of low-amplitude noise in the system, potentially from the high-speed cameras.

As mentioned at the beginning of this section, the main purpose of the CW-unforced study was to aid in the identification and attribution of the deformation response to the roughness forced synthetic mode. The forced flow perturbation has been shown to be strongly coherent in space and time and has a 2D, streamwise traveling wave structure, and so, a corresponding surface response is expected to have similar properties. From Fig. 7, features A and E do not exhibit particularly organized deformations. Feature B displays occasional streamwise wave structure, but this is intermittent and relatively low amplitude compared to the other frequency band content. Features C and D show strongly coherent traveling wave structures that are also quite energetic. However, in contrast to the expected response to the synthetic mode, C and D contain spanwise waves, and all generated waves propagate toward the center of the compliant sample. Having characterized the surface deformations with the unforced boundary layer, we now turn to the dynamic roughness forced case.

3.3 Surface response of the elastic compliant wall to a DRF turbulent boundary layer

The PSDs for the wall-normal deformation of the roughness forced deformations are shown in Fig. 9a for each FOV, corresponding to actuation condition ii ($f_f = 5$ Hz). The spectra share many of the spectral features from the unforced case shown in Fig. 6b, with the addition of a pronounced peak at 5 Hz. While the location of the f_f peak is the same for all FOVs, this peak is strongest in the TE FOV, the reason for which will be explained later. The spectra of Fig. 9a also differ in the magnitude of the low-frequency peak, corresponding to feature A (0–3 Hz) from the CW-unforced study. The amplitude of the low-frequency peak increases from LE, to corner, to TE, which is the same FOV trend for feature A of the unforced surface.

A direct comparison between the roughness forced (blue) and unforced (black) spectra is given in Fig. 9b for the LE FOV. The two agree well for spectral features C (11–16 Hz), D (18.8 Hz peak), and E (41–46 Hz). The low-frequency peaks (feature A) are colocated in f, with the forced case exhibiting a higher peak. As a note, feature A is roughly equal between the CW-unforced and CW-DRF cases for the corner FOV, and the CW-unforced peak is higher in the TE FOV, so the difference in the low-frequency peak is not strictly biased toward the forced or unforced data. The most obvious difference between the two spectra in Fig. 9b is the 5 Hz forcing frequency peak.

Fig. 9 Temporal power spectra (spatially averaged) of the compliant wall deformations in response to the DRF turbulent boundary layer (actuation condition ii). **a** Power spectra for the wall-normal deformation, d_y, in response to the DRF flow for each FOV: leading edge (blue), corner (red), trailing edge (yellow). **b** Comparison of power spectra for d_y (leading-edge FOV) in response to: CW-unforced (black) and CW-DRF (blue)
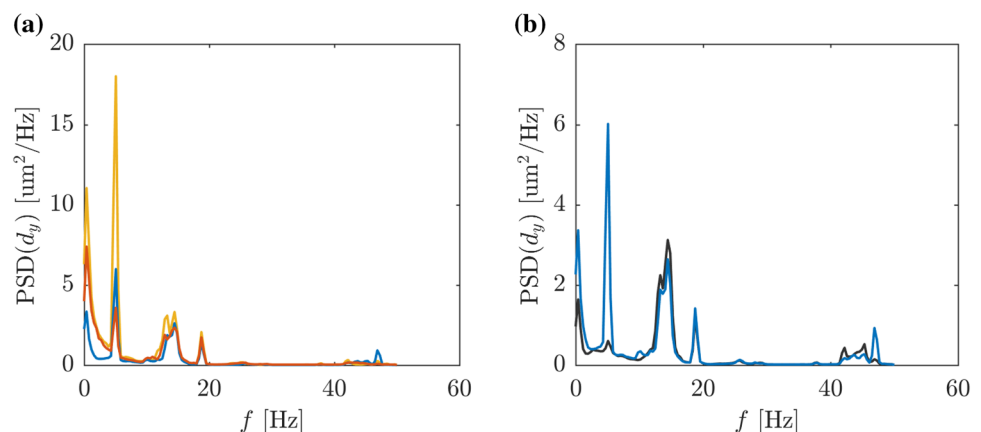
As previously discussed, though feature B (5.2 Hz peak) from the CW-unforced data resides near f_f, it is at a resolvable distinct frequency and is quite small in amplitude compared to the other features. This comparison strongly suggests that the energy injected into the system by the roughness acts primarily at the forcing frequency and does not significantly alter the energy content of the other surface modes, at least in a directly correlated manner. There does seem to be a modification of the low-frequency content, but in a non-straightforward manner. Additionally, the forcing appears to be at frequency that is otherwise relatively inactive in the surface.

To compare the spatial structure associated with the forcing frequency, the DIC data are phase-averaged and the ω_f component extracted in the same manner as the PIV velocity fields in Sect. 3.1, yielding $d_{y|\omega_f}$. Phase snapshots of $d_{y|\omega_f}$ for each FOV are given in Fig. 10. In the leading-edge FOV, nearly spanwise constant waves are observed to convect downstream, where they are slightly obscured by a background low-wavenumber, high-amplitude signal. This background content will be discussed shortly. The waves appear

largely two-dimensional, with a slight bow centered at $z = 0$. This subtle bow agrees well with the spanwise structure of the synthetic flow mode based on the previous PIV investigation (Huynh and McKeon 2019); thus, it is likely that this feature is a consequence of both the DR actuation and the panel geometry. The corner FOV is consistent with the leading edge, showing $k_z = 0$ downstream traveling waves. Notably, there are no discernible spanwise waves emanating from the side edge of the sample, as is the case in features C and D from the CW-unforced data. In the trailing-edge FOV, the streamwise traveling waves are discernible, but are significantly more obscured by a low-wavenumber signal, the likely origin of which is discussed below. It appears the bow characteristic of the waves, identified at the leading edge, has become more pronounced as the waves have convected to the trailing-edge FOV, as reflected in the increased spanwise variation in the (faint) wave signal at the TE.

In all, the data from the three FOVs describe streamwise traveling waves, with a wavelength of $\sim 2\delta$, convecting strictly downstream with a wave speed of ~ 25 cm/s or $\sim 0.7U_\infty$. The traveling wave component of the roughness

Fig. 10 The top three rows show snapshots of the temporal, ω_f Fourier mode of the wall-normal surface deformation, $d_{y|\omega_f}$, in response to the dynamic roughness forcing (actuation condition ii): (top row) trailing-edge, (second from the top) corner, (second from the bottom) leading-edge FOVs, all with contour shading limits of $[-6.0, 6.0]$ μm. The bottom row is the spatiotemporal, $\omega_f - k_{xf}$ Fourier mode for the LE data, with contour shading limits of $[-2.0, 2.0]$ μm. See supplemental material for the temporal evolution of these deformation fields
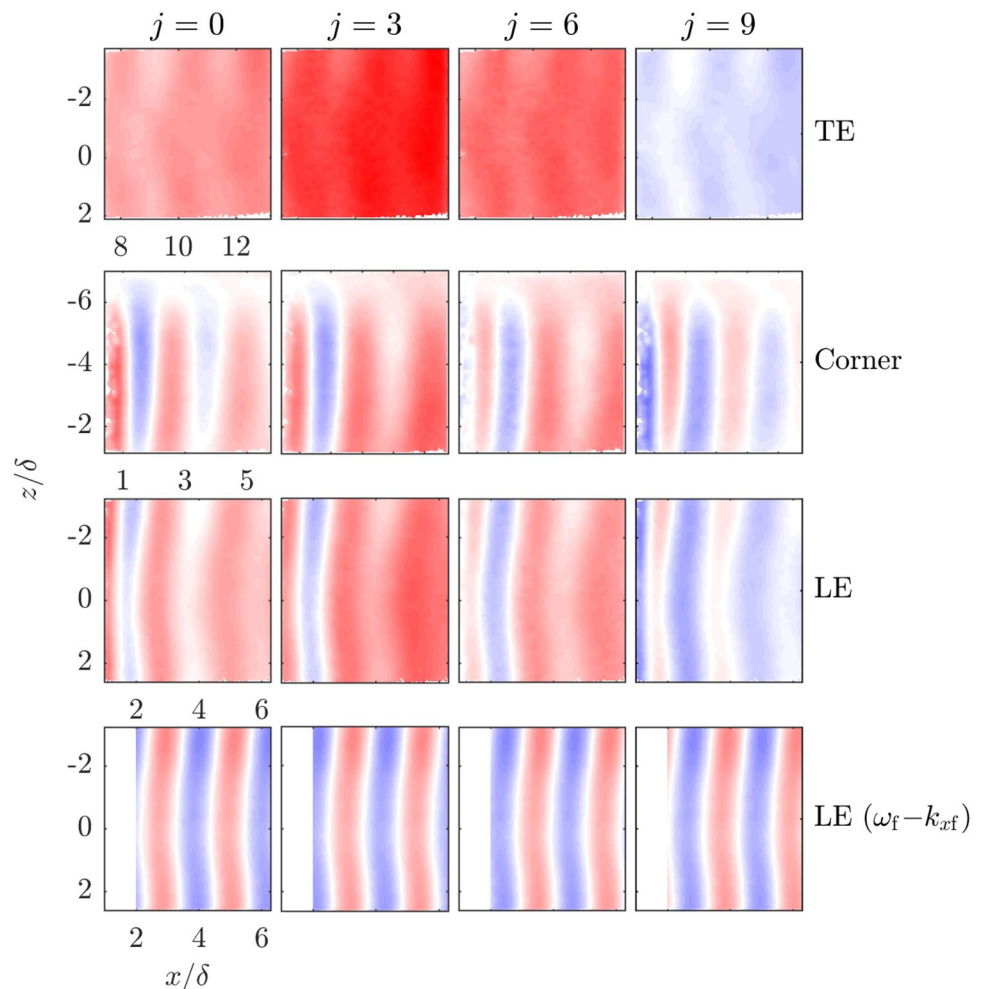
forced surface response is not consistent with any of the features from the unforced deformations and so is best attributed to direct interaction with the synthetic mode. Thus, the experiment has successfully elicited a detectable surface response to the flow structure generated by the dynamic roughness.

In addition to the deformation wave response to the roughness forcing, there was also a low-wavenumber component observed in all the FOVs. In regard to this, preliminary laser displacement measurements indicated that the compliant surface responded to the roughness actuation even when the water tunnel was off. Such a response suggests that oscillations from the roughness apparatus were somehow transmitted to the compliant surface, even with no flow. Great care was taken to completely isolate the roughness element/motor apparatus, the acrylic plate/support structure, and the camera/laser/optics from one another. In addition, the forcing frequency signature was still observed in the gelatin surface in the preliminary laser displacement data when the roughness was actuated far from the plate, with no possibility of direct contact or direct vibration transmission. Thus, quite surprisingly, it is likely that this signature is due to pressure fluctuations from the roughness element, transmitted through the water, into the acrylic, and finally to the gelatin. To characterize this response, DIC data were acquired with the roughness actuation on and the tunnel off. Though not shown here, the phase-averaged wall-normal deformation signal with the tunnel off correlates very well with the low-wavenumber content in the forced deformations, resembling the first normal mode of a vibrating membrane.

With the interaction between the synthetic flow mode and the compliant surface confirmed, the synthetic mode wavenumber, k_{xf}, was used to extract the flow forced component of the deformation response. The zero-padded DFT method (Sect. 2.3.1) was performed for $x/\delta > 2$ to avoid the transient region just downstream of the roughness and for all z. Phase snapshots of the resulting $\omega_f - k_{xf}$-coherent deformation, $d_{y|\omega_f k_{xf}}$, are shown in the bottom row of Fig. 10. Visually, the $\omega_f - k_{xf}$ component captures the traveling wave deformations well, further supporting the presence of the flow–surface interaction.

The amplitudes of the $\omega_f - k_{xf}$ Fourier coefficient for the LE and corner FOVs are plotted as functions of z in Fig. 11 to investigate any spanwise variation in the mode amplitude. The data from the two FOVs agree well in the region of overlap, and both indicate that the amplitude of the $\omega_f - k_{xf}$ response is slightly weaker along the centerline, increases toward the spanwise edge, plateaus in $-4.5 < z/\delta < -2.5$, and then decays to the edge ($z/\delta = -6$). To explore a possible reason for the bowing in mode amplitude, the k_x-amplitude spectrum is plotted in Fig. 12 for two spanwise locations, $z/\delta = 0$ and -2.8δ.

Table 5 Amplitudes and phases of the $\omega_f - k_{xf}$ wall-normal surface deformation mode and corresponding wall velocity mode for the CW-DRF study, actuation conditions ii and iii

	Case ii		Case iii	
	Amplitude	Phase	Amplitude	Phase
$\widehat{\widehat{d}}_{y|\omega_f k_{xf}}$	0.61 μm $0.2 \times 10^{-4}\delta$ $0.01\delta_v$	1.54π	1.81 μm $0.7 \times 10^{-4}\delta$ $0.03\delta_v$	1.69π
$\widehat{\widehat{v}}_{w|\omega_f k_{xf}}$	$5.3 \times 10^{-5}U_\infty$	1.04π	$1.6 \times 10^{-4}U_\infty$	1.19π

$\widehat{\widehat{d}}_{y|\omega_f k_{xf}}$ amplitudes are scaled to reflect the physical deformations and are provided in dimensional, outer-scaled, and inner-scaled forms. $\widehat{\widehat{v}}_{w|\omega_f k_{xf}}$ amplitudes are scaled to reflect the physical velocity and normalized by U_∞
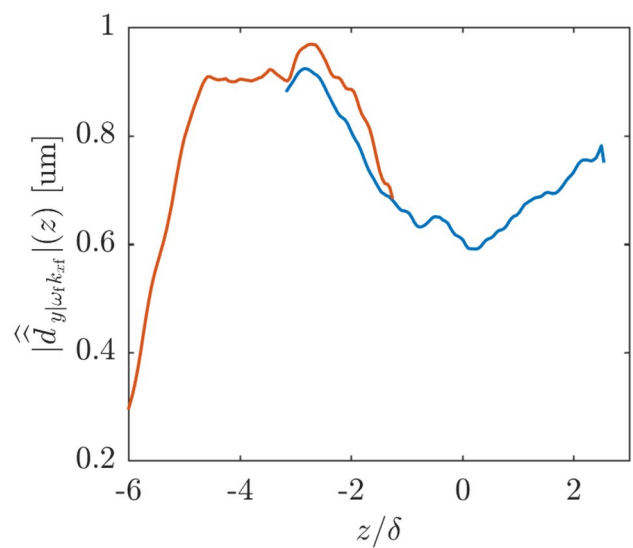

Fig. 11 Amplitude of the spatiotemporal, $\omega_f - k_{xf}$ Fourier mode of the surface deformation, $\widehat{d}_{y|\omega_f k_{xf}}$, as a function of z from the leading-edge (blue) and corner (red) FOVs. Data correspond to actuation condition ii and are scaled such that the amplitudes reflect the corresponding physical surface displacements in μm

The k_x-axis is scaled by k_{xf}. For both locations, a local peak is seen at $k_x = k_{xf}$, but the peak is notably higher in the off-center location, while the $k_x = 0$ content, related to the vibration mode, is higher in the centerline location. The inverse correlation between the $k_x = k_{xf}$ and $k_x = 0$ peaks may suggest that the strength of the vibration mode reduces the signature of the traveling wave mode. However, this could also be an effect of the spanwise edge of the compliant sample that modifies the $k_x = 0$ and $k_x = k_{xf}$ modes independently.

Even with the decreased amplitude, the $\omega_f - k_{xf}$ component of the deformation is still discernible along the centerline, and allows for an amplitude and phase of the surface response
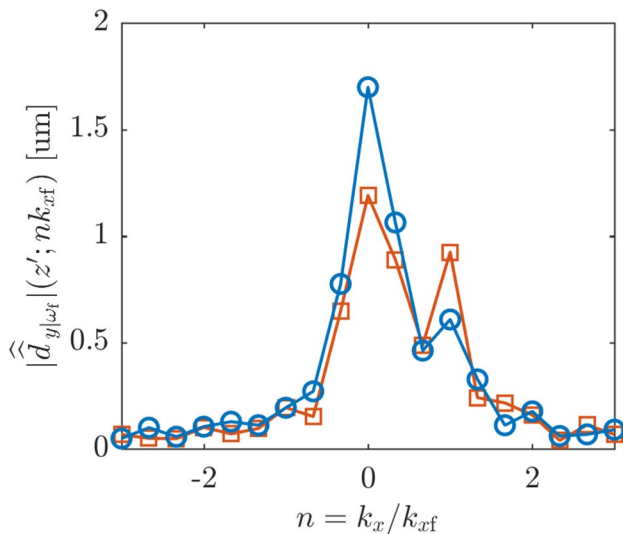
Fig. 12 k_x-amplitude spectrum for the temporal, ω_f Fourier mode of the surface deformation, $\widehat{\widehat{d}}_{y|\omega_f}$, at two spanwise locations: (blue line, circles) $z/\delta = 0$, (red line, squares) $z/\delta = -2.8$. The k_x-axis is normalized by k_{xf} to highlight the behavior of the $k_x = k_{xf}$ peak. Both sets of data correspond to actuation condition ii, are from the leading-edge FOV, and are scaled such that the amplitudes reflect the corresponding physical surface displacements in μm

mode to be defined. The amplitude and phase of the wall-normal deformation can be related to the amplitude and phase of the wall-normal velocity at the wall (v_w) by the Fourier transformed no-through flow boundary condition:

$$\widehat{\widehat{v}}_{w|\omega_f k_{xf}} = -i\omega_f \widehat{\widehat{d}}_{y|\omega_f k_{xf}} \tag{8}$$

$$\left|\widehat{\widehat{v}}_{w|\omega_f k_{xf}}\right| = \omega_f \left|\widehat{\widehat{d}}_{y|\omega_f k_{xf}}\right| \tag{9}$$

$$\angle \widehat{\widehat{v}}_{w|\omega_f k_{xf}} = \angle \widehat{\widehat{d}}_{y|\omega_f k_{xf}} - \frac{\pi}{2}. \tag{10}$$

The amplitudes and phases of the $\omega_f - k_{xf}$ wall-normal deformation and wall velocity were computed for actuation conditions ii and iii, and are given in Table 5. In both cases ii and iii, the deformation amplitude is very small, ~ 1 μm, well below 1 viscous unit. Though the amplitudes are comparable to those measured in the unforced study, it is expected that these deformations are more reliably measured due to the phase averaging process, which reduces the uncertainty of the measurement by a factor of 30 for the record lengths used here. In principle, these results can serve as a measurement of the amplitude and phase of the $\omega_f - k_{xf}$ coherent wall-normal velocity very near the wall, which would otherwise be challenging to access. This information can then be combined into the flow state of the $\omega_f - k_{xf}$ mode away

from the wall to, for example, test a model prediction of the flow–surface system response.

4 Summary and conclusions

An experiment was designed and performed to study the response of an elastic gelatin surface to the dynamic roughness forced synthetic mode in a turbulent boundary layer. Flow and surface measurements were taken via 2D-PIV and stereo-DIC, both phase-locked to the roughness motion to enable correlation between the two.

The compliant wall flow statistics were in good agreement with those of the rigid wall, suggesting that the deformations were too small to couple back to the mean flow properties. The DIC data supported this, as the wall-normal surface displacements were well below 1 viscous unit, and so, a one-way coupling was expected between the flow and surface, at least in the sense of the mean flow properties. The ω_f Fourier reconstructed velocity fields were also very similar between the RW and CW studies, though the CW supports a perturbation with slightly lower streamwise wavelength.

The wall-normal surface deformation of the CW-unforced study was analyzed to provide comparison with the CW-DRF data. The power spectrum of the CW-DRF deformations closely matched that of the CW-unforced experiment, with the addition of a strong peak at the forcing frequency, indicating that energy from the dynamic roughness was transferred to the gelatin sample. Investigating the spatial structure of the ω_f content revealed a nearly spanwise constant, streamwise traveling wave component, and a large amplitude, low-wavenumber, vibration-type component. The traveling wave signature was distinguishable from the wave features observed in the unforced surface and compared favorably with the shape of the roughness forced synthetic flow mode. Thus, the direct interaction between the synthetic mode and the compliant surface was confirmed. The vibration-type deformation that was also ω_f-coherent was suggested to be due to pressure fluctuations emanating from the roughness element, transmitted through the acrylic plate into the gelatin. This illustrates the level of sensitivity of the soft material and highlights one of the challenges faced when studying compliant surfaces with external forcing.

The LE and corner data of the $\omega_f - k_{xf}$-coherent deformation revealed that the amplitude of the mode had a convex bow shape centered at $z = 0$. As $|\widehat{\widehat{d}}_{y|\omega_f k_{xf}}|$ increases toward the spanwise edge, the $k_x = 0$ (vibration-type) mode amplitude, $|\widehat{\widehat{d}}_{y|\omega_f}|(z; n = 0)$, decreases. This may suggest an interaction between the vibration and traveling wave modes, or may simply be a spanwise edge effect. The $\widehat{d}_{y|\omega_f k_{xf}}$ component

was used to estimate the wall-normal velocity of the surface, $\widehat{\widehat{v}}_{w|\omega_{\mathrm{f}} k_{x\mathrm{f}}}$, which in turn may be related to the PIV data away from the wall to complete a near-wall/far-wall picture of the velocity mode.

What has been demonstrated here is the potential utility of dynamic roughness in compliant surface experiments. Though the interaction between the synthetic flow mode and compliant surface was verified, whether it is a one-way or two-way coupling has yet to be determined. Based on the flow statistics, one might anticipate a one-way coupling. However, an advantage of the forcing provided by dynamic roughness is that the effect on the $\omega_{\mathrm{f}}-k_{x\mathrm{f}}$-coherent synthetic mode can be isolated, and in that narrower context, a two-way interaction may yet be observed, which we consider in ongoing work.

References

Adrian R (2007) Hairpin vortex organization in wall turbulence. Phys Fluids 19(4):041301

Benschop H, Greidanus A, Delfos R, Westerweel J, Breugem WP (2019) Deformation of a linear viscoelastic compliant coating in a turbulent flow. J Fluid Mech 859:613–658

Bolt B, Butcher J (1960) Rayleigh wave dispersion for a single layer on an elastic half space. Aust J Phys 13(3):498–504

Choi K, Yang X, Clayton B, Glover E, Atlar M, Semenov B, Kulik V (1997) Turbulent drag reduction using compliant surfaces. Proc R Soc Lond Ser A Math Phys Eng Sci 453(1965):2229–2240

Czerner M, Fellay L, Suárez M, Frontini P, Fasce L (2015) Determination of elastic modulus of gelatin gels by indentation experiments. Procedia Mater Sci 8:287–296

Duvvuri S, McKeon B (2015) Triadic scale interactions in a turbulent boundary layer. J Fluid Mech 767:R4

Fernholz H, Finley P (1996) The incompressible zero-pressure-gradient turbulent boundary layer: an assessment of the data. Prog Aerosp Sci 32(4):245–311

Freund L (1998) Dynamic fracture mechanics. Cambridge University Press, Cambridge

Fukagata K, Kern S, Chatelain P, Koumoutsakos P, Kasagi N (2008) Evolutionary optimization of an anisotropic compliant surface for turbulent friction drag reduction. J Turbul 35(9):1–17

Fung Y (1965) Foundations of solid mechanics. Prentice Hall, Upper Saddle River

Gad-el Hak M (1986) The response of elastic and viscoelastic surfaces to a turbulent boundary layer. J Appl Mech 53(1):206–212

Gad-el Hak M (2002) Compliant coatings for drag reduction. Prog Aerosp Sci 38(1):77–99

Hussain A, Reynolds W (1970) The mechanics of an organized wave in turbulent shear flow. J Fluid Mech 41(2):241–258

Hutchins N, Marusic I (2007) Large-scale influences in near-wall turbulence. Philos Trans R Soc Lond A Math Phys Eng Sci 365(1852):647–664

Huynh D (2019) Spatio-temporal response of a compliant-wall, turbulent-boundary-layer system to dynamic roughness forcing. PhD thesis, California Institute of Technology

Huynh D, McKeon B (2019) Characterization of the spatio-temporal response of a turbulent boundary layer to dynamic roughness. Flow Turbul Combust. https://doi.org/10.1007/s10494-019-00069-1

Jacobi I, McKeon B (2011a) Dynamic roughness perturbation of a turbulent boundary layer. J Fluid Mech 688:258–296

Jacobi I, McKeon B (2011b) New perspectives on the impulsive roughness-perturbation of a turbulent boundary layer. J Fluid Mech 677:179–203

Kim E, Choi H (2014) Space-time characteristics of a compliant wall in a turbulent channel flow. J Fluid Mech 756:30–53

Kramer M (1957) Boundary layer stabilization by distributed damping. J Aerosol Sci 24:459

Lee T, Fisher M, Schwarz W (1993) Investigation of the stable interaction of a passive compliant surface with a turbulent boundary layer. J Fluid Mech 257:373–401

Luhar M, Sharma A, McKeon B (2015) A framework for studying the effect of compliant surfaces on wall turbulence. J Fluid Mech 768:415–441

McKeon B, Jacobi I, Duvvuri S (2018) Dynamic roughness for manipulation, control of turbulent boundary layers: an overview. AIAA J 56(6):2178–2193

Xu S, Rempfer D, Lumley J (2003) Turbulence over a compliant surface: numerical simulation and analysis. J Fluid Mech 478:11–34

Zhang C, Miorini R, Katz J (2015) Integrating Mach-Zehnder interferometry with TPIV to measure the time-resolved deformation of a compliant wall along with the 3D velocity field in a turbulent channel flow. Exp Fluids 56(11):203

Zhang C, Wang J, Blake W, Katz J (2017) Deformation of a compliant wall in a turbulent channel flow. J Fluid Mech 823:345–390

Affiliations

David Huynh[1] · Beverley McKeon[1]

David Huynh
david.huynh.58@gmail.com

[1]   California Institute of Technology, 1200 East California Blvd, Pasadena, CA 91125, USA